SUPPLEMENTAL FIGURES

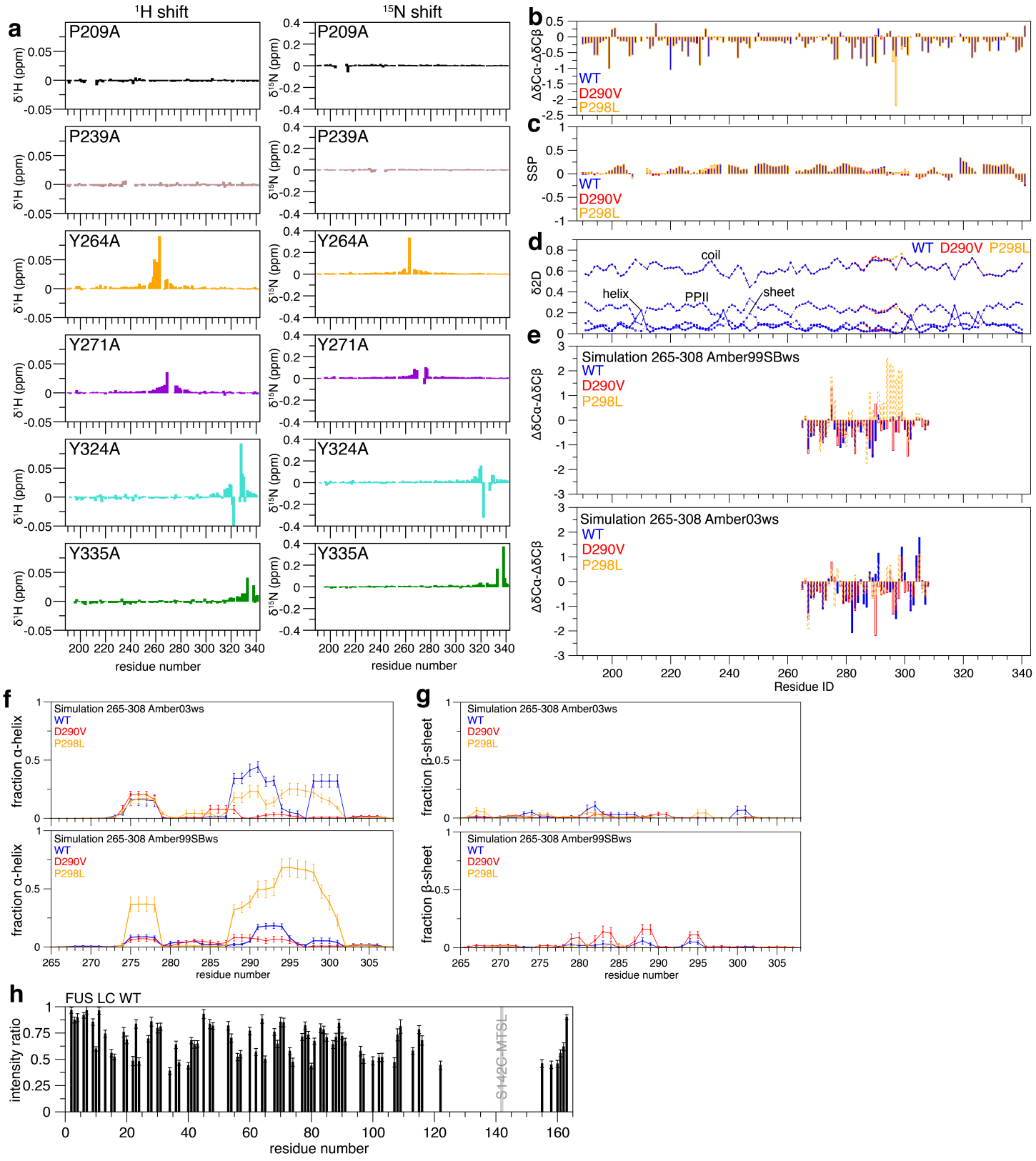

Figure S1: hnRNPA2 LC is primarily disordered. Related to Figure 1.

a) Chemical shift deviations (CSDs) for proline to alanine variants (top) are smaller than for tyrosine to alanine variants, though both are primarily local in sequence, suggesting no change in global structure. This series of variants was created to confirm NMR assignment. Shifts due to tyrosine residues may be larger than proline residues due either to larger changes in local structure for tyrosine to alanine variants compared to proline to

alanine variants, or due to large ring-current shifts produced by aromatic tyrosines, enabling observation of even transient close approach of the tyrosine to the shifted, local positions.
b) The difference between ^{13}Cα and ^{13}Cβ secondary shifts, ΔδCα- ΔδCβ, for hnRNPA2 LC are uniformly near zero, consistent with intrinsic disorder. ΔδCα- ΔδCβ and SSP show a slight change in transient local structure towards more extended structure compatible with β-sheet formation.
c) Secondary structure propensity (SSP) score values near 0 of hnRNPA2 LC indicate a lack of local secondary structure formation. Differences between WT, D290V, and P298L are localized to the regions of the mutations, showing there is a lack of global structure change in the mutant.
d) δ2D predicted secondary structure propensity also shows hnRNPA2 is primarily a random coil with slight differences between WT, D290V, and P298L in the region of the mutation.
e) Simulation of a 44-residue peptide containing the disease mutations (residues 265-308) is also primarily disordered, based on prediction of ΔδCα- ΔδCβ from the structural ensemble. Similar to the experimentally observed values, small differences in predicted ΔδCα- ΔδCβ are observed near the site of the mutation. This simulation was performed in both the Amber03ws and Amber99SBws force fields.
f-g) Secondary structure population as calculated by DSSP from the simulation ensemble indicate that the small differences in ΔδCα- ΔδCβ caused by the D290V mutation is consistent with a shift in minor population of α-helix **(f)** to β-sheet **(g)**. As the proline to leucine mutation is not well modeled by the Amber99SBws force field we had previously used as evidenced by the large increase in α-helical content not observed by experiment, we simulated all three peptides in both Amber99SBws and Amber03ws, which showed significantly less helical structure stabilization for P298L.
h) FUS intramolecular PREs as calculated by HSQC intensity ratio show that hnRNPA2 LC is more collapsed than a similar low complexity domain.

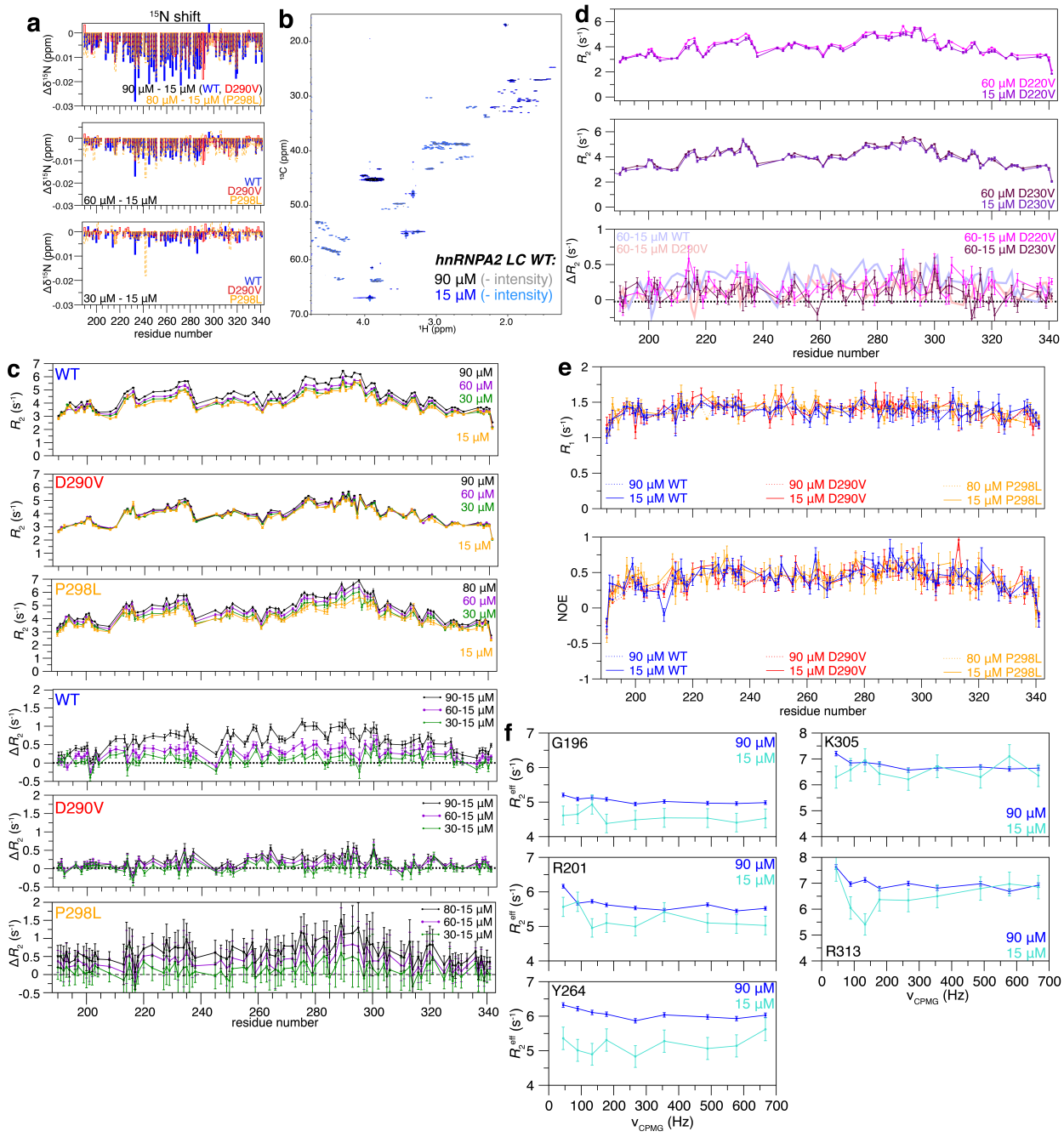

Figure S2: hnRNPA2 LC forms intermolecular interactions. Related to Figure 2.

a) Small chemical shift deviations (CSDs) are observed for backbone ^{15}N positions as a function of increasing protein concentration for WT, D290V, and P298L. ^{15}N CSDs for D290V as a function of concentration are greatest in magnitude near D290V, suggesting D290V self-interaction may occur more frequently at this position. Comparing the highest and lowest concentrations, WT shows larger ^{15}N shifts on average than D290V or P298L, suggesting WT forms more transient intermolecular interactions than D290V (see Figure 2).

b) ^{1}H-^{13}C constant time HSQC of WT LC at 90 μM (positive and negative contour intensities in black and grey respectively) and 15 μM (positive and negative contour intensities in blue and cyan) show no significant chemical shift perturbations.

c) As the concentration decreases, the R_2 for hnRNPA2 WT LC decreases. D290V shows a slight decrease in R_2 with decreasing concentration, but much less than WT. P298L shows a similar decrease in R_2 as compared to WT. This ΔR_2 indicates that the WT and P298L proteins are forming intermolecular interactions.

d) To determine if the difference in R_2 as a function of concentration for WT and D290V arises due to net charge differences, two other D to V mutations introduced at engineered D220V and D230V positions were

created. R_2 at 60 μM and 15 μM shows that D220V and D230V are more similar to D290V than WT suggesting that the loss of the negative charge plays a role in reducing the intermolecular interactions.
e) ^{15}N R_1 and heteronuclear NOE do not change as a function of concentration for WT, D290V, or P298L.
f) Apparent ^{15}N R_2 as a function of applied CPMG field, ν_{CPMG}, measured at 90 μM and 15 μM show very slight relaxation dispersion in high concentration samples. Some residues (G196, R201, Y264, K305, R313) with the highest dispersion are shown. This dispersion is less than 1 s^{-1} and is not always significantly different from the profiles observed for the low concentration sample.

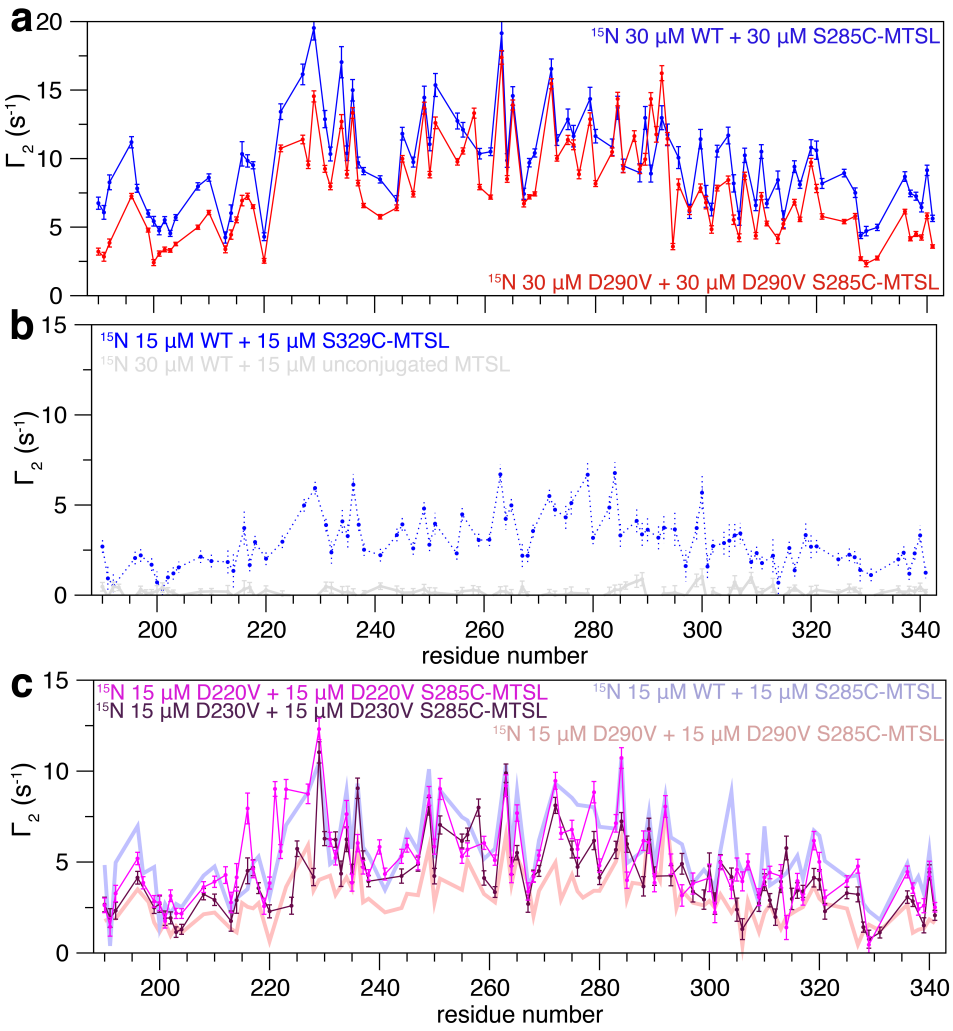

Figure S3: hnRNPA2 LC forms transient intermolecular interactions. Related to Figure 2.
a) Intermolecular paramagnetic relaxation enhancement values, Γ_2, observed for mixtures of 30 μM ^{15}N protein with 30 μM spin-labeled protein are larger than those for 15+15 μM (Figure 2C) showing that intermolecular interactions increase with increasing concentrations.
b) Intermolecular PREs performed with an unconjugated MTSL are near 0, showing that the spin label must be conjugated to hnRNPA2 LC to give rise to the PREs observed for both S285C and S329C (plotted for comparison).
c) Intermolecular PREs for engineered D to V variants D220V (magenta) and D230V (purple) are intermediate between WT (blue outline, repeated from Figure 2C for clarity) and D290V (red outline), indicating the change in residue at location 290 is critical for the difference observed in intermolecular PREs.

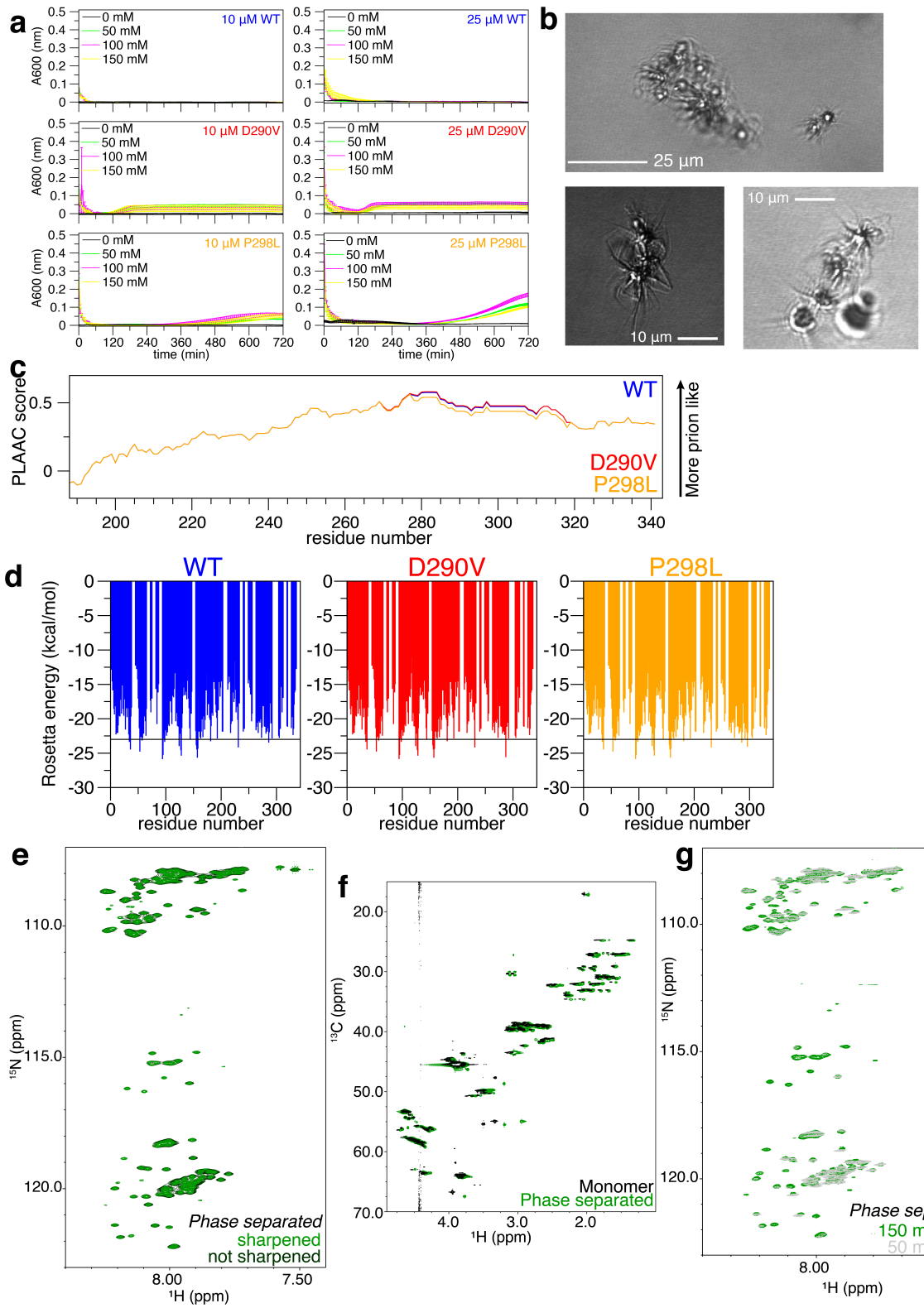

Figure S4: Phase separation and aggregation of hnRNPA2. Related to Figures 3 and 4.
a) After initiating phase separation, turbidity of WT hnRNPA2 LC samples decreases steadily to zero, consistent with the reduction in number of droplets observed by microscopy (see Figure 3c). Conversely, turbidity of D290V hnRNPA2 LC initially decreases but stabilizes at a non-zero value, consistent with formation of stable aggregates not observed for WT. P298L shows a similar reduction in turbidity to WT initially but then at later time points (after ~6 hours), the turbidity increases again, consistent with the formation and enlargement of aggregates.

b) At 3 hours after droplet formation, D290V forms large aggregates that appear as though droplets failed to fuse and have fibrils coming out of them, as observed previously for FUS.
c) PLAAC (Lancaster et al. 2014) scores for the 190-341 region of hnRNPA2 WT, D290V, and P298L. P298L decreases prion propensity for the region of the mutation while D290V slightly increases it.
d) ZipperDB (Thompson et al. 2006) graphs for the full length hnRNPA2 show no differences except in the regions of the mutations.
e) Comparison of line sharpened and standard processing of HSQC spectra of hnRNPA2 LC demonstrates that line sharpening improves resolution without altering the spectrum of the phase-separated state.
f) ^{1}H-^{13}C real time HSQCs of the monomer (black) and phase separated (green) hnRNPA2 LC show no major differences, further indicating that the NMR-visible segments of phase-separated LC do not adopt a different predominant secondary structure than that of the dispersed monomer.
g) Overlay of HSQCs of phase-separated WT LC made in 150 mM NaCl and 50 mM NaCl show minor differences, indicating the salt concentration does not qualitatively change the structure or spectral properties of the phase separated state.

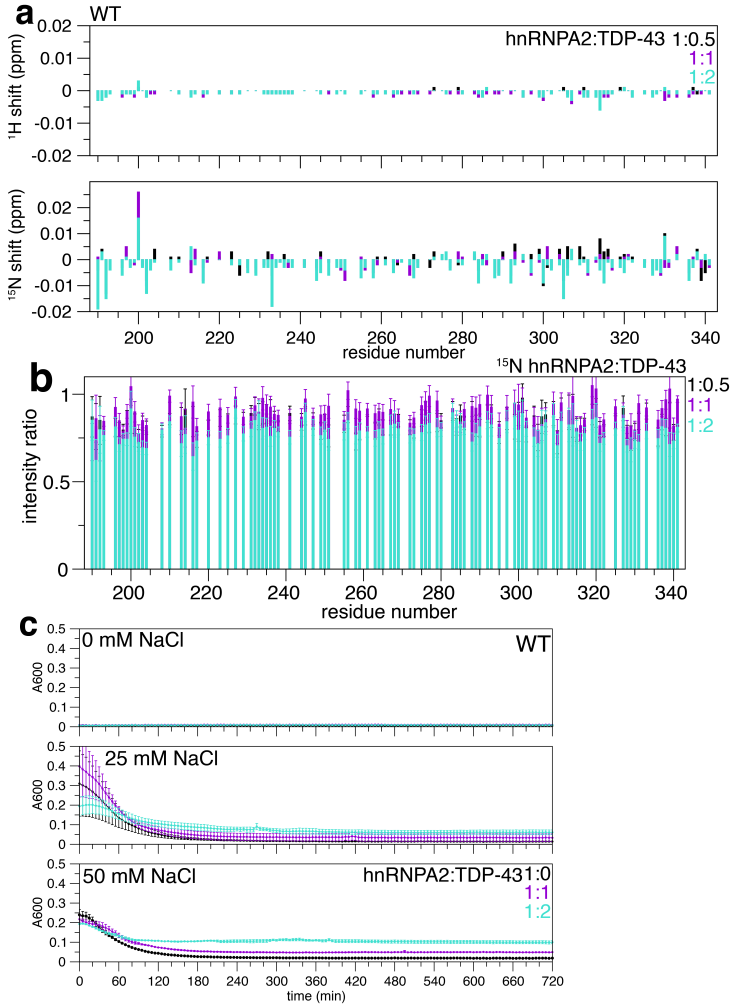

Figure S5: hnRNPA2 interacts and TDP-43. Related to Figure 5.
a) WT hnRNPA2 LC shows small chemical shift perturbations in the presence of TDP-43 CTD indicative of weak binding.
b) Addition of TDP-43 CTD induces a uniform loss of signal intensity of hnRNPA2 LC resonances, consistent with interactions across the entire domain or incorporation into high molecular weight species.
c) Over time, turbidity values for WT hnRNPA2 LC mixed with TDP-43 CTD reach a plateau, consistent with the presence of a stable aggregated species. With increasing TDP-43, the turbidity also increases, indicating that TDP-43 may aggregate itself or with hnRNPA2 LC.

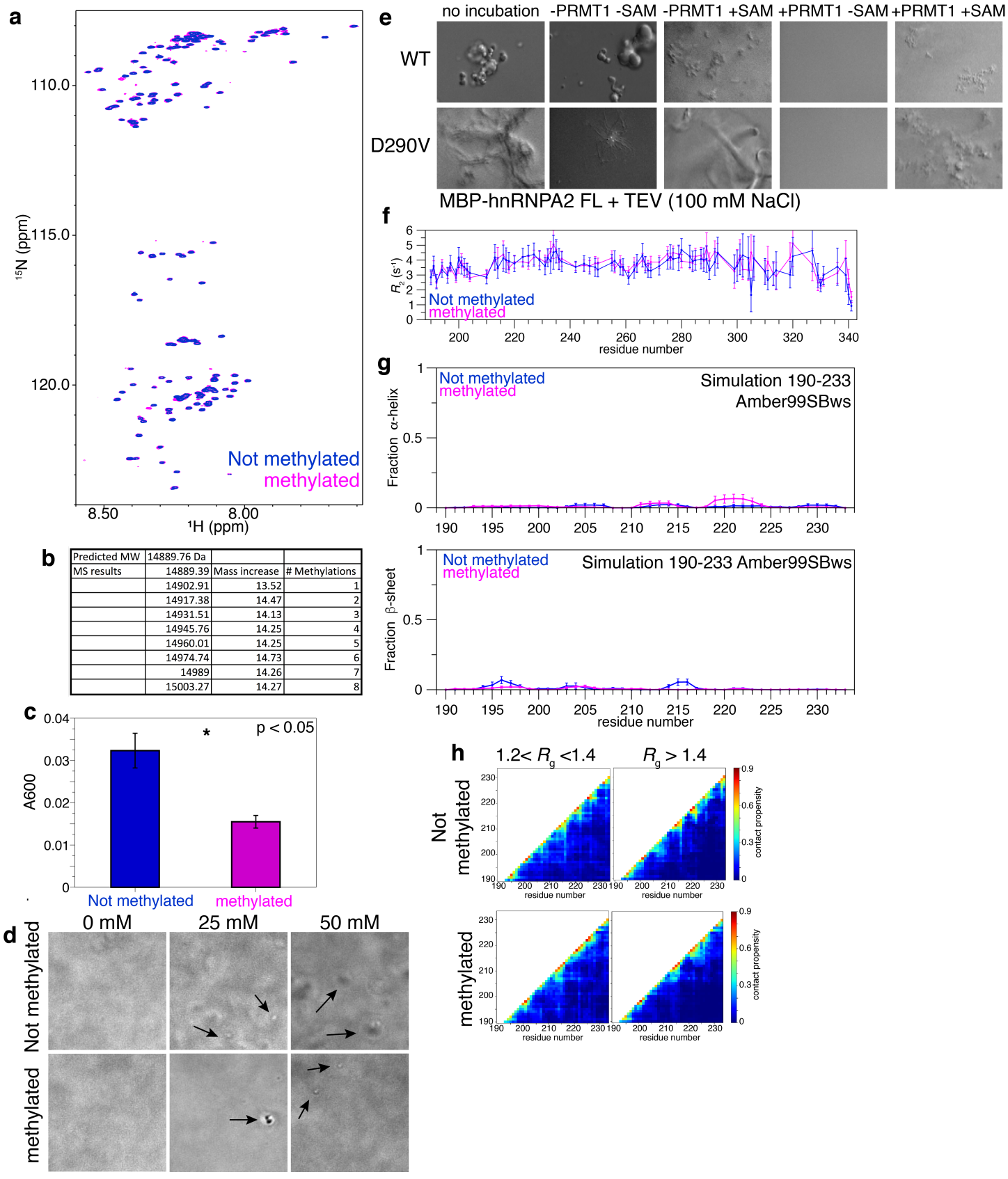

Figure S6: hnRNPA2 LC is methylated *in vitro* by PRMT1. Related to Figure 6.

a) Full backbone ^{1}H-^{15}N HSQC spectra of methylated and unmethylated hnRNPA2 LC shows minor chemical shift deviations at peaks in or near RGG motifs and no shifts elsewhere as expected for methylation. Both the methylated product and the control reaction lacking PRMT1 (-PRMT1) were purified under denaturing

conditions to remove all enzyme and reaction mixture components so chemical shifts do not reflect PRMT1 binding to hnRNPA2 LC.
b) Table showing the increases in mass after incubation of hnRNPA2 LC with PRMT1. A single methylation corresponds to an increase of about 14 Dalton.
c) Turbidity of hnRNPA2 LC methylated by PRMT1 (magenta) is decreased compared to a mock reaction lacking PRMT1 (blue), after the MBP-attached hnRNPA2 LC is cleaved from MBP by TEV and re-purified in denaturing conditions to remove the His-tagged PRMT1, His-tagged MBP, and His-tagged TEV.
d) Microscopy images of methylated and unmethylated hnRNPA2 LC show spherical structures in 25 mM and 50 mM NaCl, consistent with phase separation.
e) After the incubation required for PRMT1 methylation, full length hnRNPA2 no longer phase separates, precluding assays to assess the effect of methylation on phase separation of the full length protein.
f) ^{15}N R_2 measurements for methylated and un-methylated hnRNPA2 LC (approximately 10 μM, 150 mM urea) show no difference and thus cannot explain the difference observed in phase separation.
g) In a simulation of hnRNPA2 190-233, the fraction of α-helix and β-sheet do not substantially change between the methylated and unmethylated peptides.
h) Contact maps from the simulations for mid and high R_g do not look substantially different between methylated and unmethylated hnRNPA2 LC.